An Imaging Technique for Safe Spacecraft Landing and Autonomous Hazard Avoidance

Brandon M. Jones, *Student Member, IEEE*
Electrical Engineering Department
Southern University and A&M College
Baton Rouge, LA 70813, USA

Ayanna Howard, *Senior Member, IEEE*
Human-Automation Systems Laboratory
Georgia Institute of Technology
Atlanta, GA 30332, USA

Abstract

The focus of this paper is to present an image transformation algorithm to interpret historical imagery land data for autonomous safe landing of a robotic spacecraft. Inherent geographical hazards of Martian terrain may impede safe landing for a science exploration spacecraft. Surface visualization software for hazard detection and avoidance may therefore be applied to enable an autonomous and intelligent spacecraft descent upon entering the planetary atmosphere. The methodology proposed involves integrating linear algebra and computer vision/graphics techniques, with the intrinsic parameters governing spacecraft dynamic motion and camera calibration, in order to assess hazards that might impede spacecraft landing. In this paper, we provide algorithmic details and simulation results of our methodology applied to a representative Mars landing descent profile.

Keywords – Computer Vision, Coordinate Systems, Projective Geometry, 3D Rotation Matrix, Linear Algebra

1. Introduction and Background

The focus of future Mars exploration missions will involve the autonomous satisfaction of three critical post launch events prior to science exploration: *entry* into the planetary gravity field and atmosphere, *descent* through that atmosphere towards a region of scientific interest and priority constrained by engineering influence, and *landing* such that the integrity of onboard instrumentation is preserved. The heritage design of this critical entry, descent, and landing (EDL) procedure involves visual human inspection of the Mars surface using various imaging techniques and past mission data prior to atmospheric entry for landing site predetermination [1-3]. Our research aims to produce a cognitive descent by the spacecraft through the mid to lower atmosphere by introducing vision techniques and low cost algorithms to autonomously perform real-time hazard assessments based on features of the terrain realized through camera imagery. Introducing such a technique for EDL in the absence of human interaction includes the benefit of the camera as a low-cost flight-credible spacecraft sensor for use in computing and processing complex yet safe and accurate descent trajectories [4].

Certain analytical image processing methods – such as crater, rock, and shadow detection – are available for the robotic recognition and reach determination of safe surface coordinates based on surface imagery [5-6]. Other techniques implement homography to transfer features between two simultaneous camera scenes separated in space, but negligent of time [7-8]. We integrate concepts from each technique with various methods in computer vision and linear algebra to produce a low-cost algorithm for autonomous hazard avoidance. Currently there is no internal comparison of early-descent images to those taken further in descent. Our hazard assessment approach involves applying an image transformation algorithm and developing a correlation scheme that allows historical imagery data to be incorporated for hazard assessment during spacecraft descent. Due to the angle at which sensors are mounted on the spacecraft, the swath, or scene plane, will be in perspective relative to the mounting angle and camera field of view (FOV). Image registration occurs by translating the image taken at one instance in time into a more suitable coordinate system during the time delta between imaging. This research focuses on comparing current imagery data with former, midway, and latter descent hazard information to reduce the error for image comparison.

2. Technique

2.1 Developing a Camera Model for Spacecraft Descent

In this paper we develop an image registration methodology to achieve a computationally low-cost descent algorithm for the purpose of robotic spacecraft landing in the absence of human interaction. We define a digital image as a quantitative set of discrete data units of a visual observation perceived by a sensing element, or camera. For cameras, this data set consists of a band of light intensities varying throughout the visible frequency spectra representative of points on a viewing surface. We model the viewing surface as a normalized digital elevation model (DEM) to simulate surface normal vectors for rough terrain (Figure 1).

2nd IEEE International Conference on Space Mission Challenges for Information Technology (SMC-IT'06)
0-7695-2644-6/06 $20.00 © 2006 IEEE

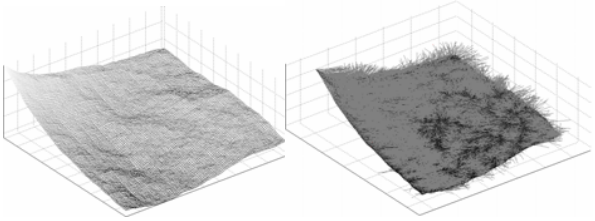

Normalized DEM Surface Normal Equivalent

Figure 1 Graphical simulation of rough terrain (left) and surface normal plot (right)

Incident light originating from the light source position $\boldsymbol{\omega}$ provides a virtual illumination of the DEM. This energy model simulates light radiated towards points on the DEM surface to exhibit a luminous flux for each respective point. This allows us to characterize an arbitrary surface coordinate by extracting the local angle of incidence formed between the unit surface normal vector and the directed light energy unit vector for any given coordinate located on the virtual terrain [9]. We use the dot product equivalent of this occurrence to form the following pixel intensity equation, which allows us to produce an artificial depth model for surface hazard assessment:

$$I = \mathbf{n}_{\mathrm{u}}^{\mathrm{T}} \cdot \boldsymbol{\omega}_{\mathrm{u}} \left(2^{n} - 1\right) \qquad (1)$$

The image control enumeration n supplements the scalar intensity I and defines the image architecture, which is composed of the surface normal unit vector $\mathbf{n}_{\mathrm{u}}$ of a given DEM coordinate and the radiated light unit vector $\boldsymbol{\omega}_{\mathrm{u}}$ of the luminous source. Each of these Cartesian vectors consists of an x, y, and z component: $\mathbf{n}_{\mathrm{u}} = [n_x \;\; n_y \;\; n_z]^{\mathrm{T}}$ and $\boldsymbol{\omega}_{\mathrm{u}} = [\omega_x \;\; \omega_y \;\; \omega_z]^{\mathrm{T}}$. We use the T operator to transpose the 3×1 $\mathbf{n}_{\mathrm{u}}$ operand to form a discrete and descriptive scalar quantity between each vector. The geometry of $\mathbf{n}_{\mathrm{u}}$ and $\boldsymbol{\omega}_{\mathrm{u}}$ causes a pixel intensity of zero in the event of a perpendicular orientation between the two vectors. We use Equation (1) to assign an array of 2^n pixel shades ranging from a "right angle" unit vector occurrence value of zero to a nonzero value correlating to a 2^n-1 color scale for an n-bit color scheme.

We represent a static DEM coordinate as $\mathbf{x} = [x \;\; y \;\; z]^{\mathrm{T}}$ and the dynamic spacecraft position by $\mathbf{p} = [p_x \;\; p_y \;\; h]^{\mathrm{T}}$, where h is the decaying altitude relative to $\mathbf{x}$ due to spacecraft descent, as shown in Figure 2. Each 3D world coordinate $\mathbf{x}$ integrated within a DEM test-bed is designed to exhibit *safe*, *risky*, and *unsafe* geographical features using a fractal terrain algorithm. *Safe* landing sites are surface regions relatively free of detectable geographic hazards including edges, steep slopes, rocks, and craters. *Risky* landing sites constitute areas less suitable for spacecraft landing and science exploration. *Unsafe* landing sites have the highest probability of mission failure due to geographic hazards. In Section 2.5, we discuss the calculation of each hazard type using a methodology based on Equation (1).

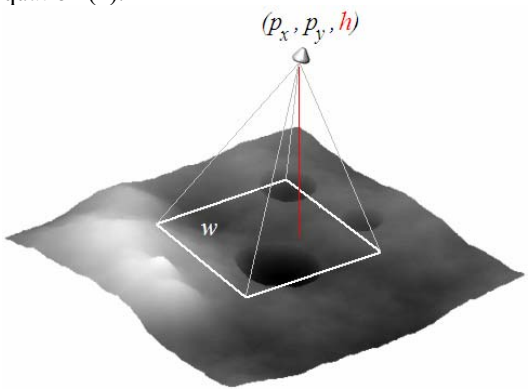

Figure 2 Instantaneous coverage frustum graphic at spacecraft altitude h above DEM with viewing plane w within the imager FOV

The dynamics of this simulation involves the creation of a vision scenario such that a descent profile from the perspective of the vehicle is accomplished. It includes approximating camera coverage area of the terrain by observing the tangential geometry between the scene plane w, spacecraft altitude h, and camera FOV.

$$W = 2h \tan\left(\frac{\mathrm{FOV}}{2}\right) \qquad (2)$$

The coverage area of the camera swath shown in Figure 2 within the w plane consists of four equal sides of width W. A camera image of this area is based on the various pixel intensities associated with corresponding DEM surface coordinates. Intensity projections of these coordinates are stored to form an image intensity matrix emulative of a camera charge coupling device (CCD) using Equation (1). The camera calibration parameters, such as the focal length f, resolution c, and principle point (image center) at coordinate (u_0, v_0) are also included using a form of the pin-hole calibration matrix $\mathbf{K}$ for image projection [10-12].

$$\mathbf{K} = \begin{bmatrix} fc & 0 & u_0 \\ 0 & fc & v_0 \\ 0 & 0 & 1 \end{bmatrix} \qquad (3)$$

This homogeneous calibration matrix is significant for camera simulation as it contains those intrinsic and generic parameters characteristic of camera based flight hardware.

2.2 Modeling the Spacecraft Descent Profile

A spacecraft descent trajectory during EDL through an atmosphere consists of various rotational and translation coefficients. To create a vision scenario such that the

effect of descent from the camera perspective is accomplished, we transform each DEM coordinate via numeric shifting and rigid rotation. We incorporate the following 3D graphical rotational matrices for a non-flight EDL simulation model:

$$\mathbf{R_x} = \begin{bmatrix} 1 & 0 & 0 \\ 0 & \cos\theta_x & -\sin\theta_x \\ 0 & \sin\theta_x & \cos\theta_x \end{bmatrix} \quad (4)$$

$$\mathbf{R_y} = \begin{bmatrix} \cos\theta_y & 0 & \sin\theta_y \\ 0 & 1 & 0 \\ -\sin\theta_y & 0 & \cos\theta_y \end{bmatrix} \quad (5)$$

$$\mathbf{R_z} = \begin{bmatrix} \cos\theta_z & -\sin\theta_z & 0 \\ \sin\theta_z & \cos\theta_z & 0 \\ 0 & 0 & 1 \end{bmatrix} \quad (6)$$

Equations (4-6) are used to produce rigid DEM rotation of θ_x, θ_y, and θ_z radians about the x, y, and z axis, respectively, for each virtual terrain coordinate. Using basic matrix multiplication we concatenate Equations (4-6) to form a single orthogonal matrix **R** that is characteristic of rotation about each axis in a singular form. Using Equation (3) we are able to fully transform a DEM coordinate for imaging purposes taking into account the position and orientation of the spacecraft:

$$\mathbf{x}' = \mathbf{KRx} + \mathbf{p} \quad (7)$$

where $\mathbf{x}'$ is the new DEM coordinate as it relates to movement by the spacecraft at an *arbitrary* position and altitude in space, **K** is the homogeneous calibration matrix and **p** is the spacecraft position vector. This non-flight 3D equation is used as a setup for the development and simulation for our 2D autonomous software algorithms to be performed on-board the spacecraft.

2.3 Extracting Camera Descent Imagery from 3D Terrain Models

We collect 3D coordinate system data from our surface model test-bed to form a homogenized 2D representation of a DEM using Equation (7). For a world coordinate $\mathbf{x}'$ of the form $\mathbf{x}' = [x' \;\; y' \;\; z']^{\mathrm{T}}$ there exist a corresponding retinal image coordinate denoted as $\mathbf{u} = [u \;\; v \;\; 1]^{\mathrm{T}}$ [13]. The scalar pixel components of vector **u**, algebraically denoted as $u = x'/z'$ and $v = y'/z'$, are perspective projections of the amalgamation $\mathbf{x}'$. These 2D image coordinates – functions of the spacecraft position, camera parameters, and DEM orientation – are used in algorithmic conjunction with Equation (1) to produce an *n*-bit shaded image of world coordinates within the camera FOV. Rotational and translation operations are applicable to the resulting 2D imagery extracted from surface data, as shown in Figure 3.

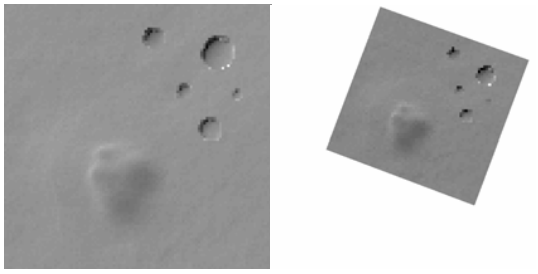

Figure 3 Original DEM image (left) and transformed image (right) via rotational and translation coefficients

The imagery exhibited above in Figure 3 reflects an overhead camera FOV for a particular DEM. We denote an initial image produced directly from a 3D coordinate system as IM_i. Producing an initial image IM_i composed of an array of **u**-coordinates requires the use of Equation (3) to account for the intrinsic parameters of the camera model. Once produced and stored IM_i exist as a qualitative byproduct of the spacecraft camera. It follows that in the rotation and translation of a 2D image coordinate that camera calibration no longer exists as a coordinate system transform requirement. The transformation shown in Figure 3 is accomplished using the following 2D version of Equation (7) implicitly inclusive of **K**:

$$\mathbf{u}' = \mathbf{Ru} + \mathbf{p} \quad (8)$$

where $\mathbf{u}'$ is the new image coordinate as it relates to movement by the spacecraft due to a *previous* position and altitude in space. This equation is the non-homogenous transformation for a two-space image **u**-coordinate of the following vector form: $\mathbf{u}' = [u' \;\; v' \;\; w]^{\mathrm{T}}$. Using Equation (8) we derive the homogenous argument $\mathbf{u}'' = [u'' \;\; v'' \;\; 1]^{\mathrm{T}}$ containing the pixel components $u'' = u'/w$ and $v'' = v'/w$. Through simulation, an array of $\mathbf{u}''$ pixel coordinates is used to produce a second generation image transform IM_T from an augmented **u**-coordinate IM_i or IM_{i+1} system, where IM_{i+1} is a second camera image taken further in descent. We adopt nomenclature for the original DEM image and transformed image in Figure 3 as IM_i and IM_T, respectively. Parameters for consecutive 3D surface imagery collected by the spacecraft for each respective altitude *h* are assigned:

$$\{u_i, v_i, z_i\} \in IM_i \quad (9)$$

$$\{u_{i+1}, v_{i+1}, z_{i+1}\} \in IM_{i+1} \quad (10)$$

where z_i and z_{i+1} are the corresponding and respective spacecraft altitudes for the camera images IM_i and IM_{i+1}. Equations (9-10) are the fundamental image sets used for our descent profile registration methodology.

2.4 Registering Multi-Plane Descent Imagery

Descent imagery consists of a *finite* quantitative set of discrete two-space **u**-coordinate data correlating to a three-space visual observation of corresponding **x**-coordinates perceived by the spacecraft camera. By applying a translation transformation scheme using Equation (8), an initial image IM_i may be transformed to produce a new image IM_T reminiscent of the root image IM_i yet displaced into a new coordinate system. The original camera image coordinate system prior to 2D transformation and formation of IM_T contains a complete **u**-coordinate pixel set collected from an initial altitude z_i within the camera FOV. For such a planar transformation, a negated Equation (8) may be reapplied to image IM_T. This causes a special transformation resulting in the registration of the transformed image IM_T into the coordinate system of the root image IM_i, as shown below in Figure 4.

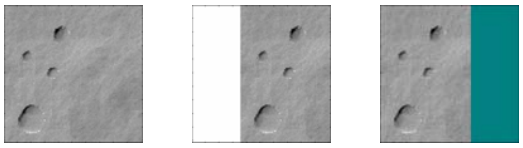

Image IM_i Transform IM_T Reverted IM_T

Figure 4 Planar image translation and pixel truncation (■) by reverse registration of image IM_T to IM_i

Registration involves the matching of a captured image in one coordinate system to another image of a different coordinate system. The special transformation shown above is the reverse registration of image IM_T to the initial image IM_i resulting in a new image IM_r. By observing IM_r in Figure 4 (Reverted IM_T), we find that pixels originally present within the original coordinate system are lost during the registration process of the transformed image IM_T to the destination coordinate system containing IM_i. Registration of 2D imagery between planar coordinate systems thus presents a trade-off between the use of image transformation and **u**-coordinate retention for a descent profile. Using Equation (9-10) nomenclature IM_T is the essential equivalent of image IM_{i+1}, constituting IM_i and IM_T as a planar fundamental image set non-variant in altitude. A multi-plane registration methodology for an initial image IM_i and an iterated image IM_{i+1} taken further in descent is desirable for the robotic analysis of historic EDL imagery.

Special application of Equation (8) results in the registration of an object image in one coordinate system to another image containing intersecting data to the object, but from the perspective of a different coordinate system. This new perspective in EDL is due to a descending change in spacecraft position **p** through an atmosphere. The initial spacecraft image IM_i correlates to scene plane data within the camera FOV at position $\mathbf{p_i} = [p_{x,i} \;\; p_{y,i} \;\; z_i]^T$. A consecutive spacecraft image IM_{i+1} correlates to scene plane data within an intersecting FOV extracted at position $\mathbf{p_{i+1}} = [p_{x,i+1} \;\; p_{y,i+1} \;\; z_{i+1}]^T$, where z_{i+1} is less than z_i for a descent profile and spacecraft positions $\mathbf{p_i}$ and $\mathbf{p_{i+1}}$ are 3D world coordinates. We use Equation (2) as a linear transfer function between 3D world coordinates $\mathbf{p_i}$ and $\mathbf{p_{i+1}}$ correlating to the projective 2D image coordinates $\mathbf{u_i}$ and $\mathbf{u_{i+1}}$, respectively.

Table 1. Swath width as a function of spacecraft altitude for linear derivation of pixel translation

Position	*W*(*h*)	*Pixel Translation*
$p_{x,i}$	$h = z_i$	$u_i = p_{x,i} / W(z_i)$
$p_{y,i}$	$h = z_i$	$v_i = p_{y,i} / W(z_i)$
$p_{x,i+1}$	$h = z_{i+1}$	$u_{i+1} = p_{x,i+1} / W(z_{i+1})$
$p_{y,i+1}$	$h = z_{i+1}$	$v_{i+1} = p_{y,i+1} / W(z_{i+1})$
$\{W(z_i), W(z_{i+1})\} \neq 0$		

This provides an equivalent pixel translation scheme given the dynamic position **p** of a descending spacecraft relative to a static DEM coordinate **x** (Table 1). In developing a multi-plane registration methodology we analyze the fundamental set of imagery taken by the spacecraft at positions $\mathbf{p_i}$ and $\mathbf{p_{i+1}}$. By assigning the initial fundamental image IM_{i+1} captured at position $\mathbf{p_{i+1}}$ by the spacecraft as a transformation object, we achieve the reverse registration of IM_{i+1} to the coordinate system of IM_i captured at position $\mathbf{p_i}$ by substituting a difference scheme into Equation (8):

$$u_r = u_i \frac{z_i}{z_{i+1}} - u_{i+1} \tag{11}$$

$$v_r = v_i \frac{z_i}{z_{i+1}} - v_{i+1} \tag{12}$$

$$z_r = \frac{z_i - z_{i+1}}{z_{i+1}} \tag{13}$$

$$z_{i+1} \in \{u_r, v_r, z_r\} \neq 0 \tag{14}$$

Equations (11-13) are registration coordinates for the object image IM_{i+1} extracted from an altitude of z_{i+1} to the coordinate system of image IM_i taken earlier in descent at altitude z_i. The reverse registration of IM_{i+1} to the initial

image IM_i results in a new image transformation IM_r. Conversely, by assigning the fundamental image IM_i captured at position $\mathbf{p_i}$ by the spacecraft as a transformation object, we achieve the forward registration of IM_i to the coordinate system of a second image IM_{i+1} captured at position $\mathbf{p_{i+1}}$ by substituting a similar difference scheme into Equation (8):

$$u_f = u_{i+1}\frac{z_{i+1}}{z_i} - u_i \tag{15}$$

$$v_f = v_{i+1}\frac{z_{i+1}}{z_i} - v_i \tag{16}$$

$$z_f = \frac{z_{i+1} - z_i}{z_i} \tag{17}$$

$$z_i \in \{u_f, v_f, z_f\} \neq 0 \tag{18}$$

Equations (15-17) are registration coordinates for the object image IM_i extracted from an altitude z_i to the coordinate system of image IM_{i+1} taken further in descent at altitude z_{i+i}. The forward registration of IM_i to the consecutive image IM_{i+1} results in a new image transformation IM_f. Visual examples of 2D forward and reverse registration are shown below in Figure 5.

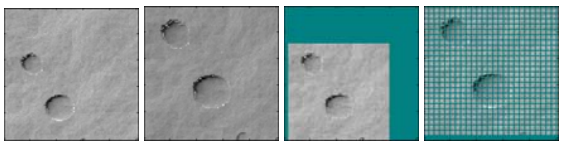

IM_i IM_{i+1} IM_r IM_f

Figure 5 Registration simulation of consecutive spacecraft imagery for two spacecraft perspectives of a DEM

The initial spacecraft image contains a complete pixel set collected from the first imaging altitude z_i within the camera FOV. In IM_i of Figure 5, two craters on the DEM are in view of the camera perspective. As the spacecraft descends to extract a second image IM_{i+1}, the same craters remain located in the camera FOV. However, due to the new perspective of the spacecraft, the craters appear larger. Using reverse registration, we compare the most recent EDL surface image IM_{i+1} to the previous image IM_i by translating the latter image into the coordinate system of the former perspective, resulting in image IM_r. Surface data surrounding IM_r, previously unavailable from the spacecraft perspective, is shown above as an empty set of data (■). In forward registration we compare a former EDL surface image IM_i to a latter image IM_{i+1} by translating the former into the coordinate system of the latter perspective, resulting in image IM_f. The truncated data spread (■) permeated throughout the forward registered image in Figure 5 is due to an unavailability of lower atmosphere surface data in the registration process. Each methodology involves a tradeoff between the benefit of the registration process and pixel retention due to varying perspectives of the spacecraft camera.

2.5 Assessing Hazardous 3D Terrain Geography

In this section we present a statistical method to develop a rule set for real-time hazard assessment of terrain geography through influence of an intensity based algorithm [14]. Figures 3-5 originate from virtual spacecraft imagery of size $i \times j$ from a world scene plane w during an instance of descent towards a fractal terrain model. We define specialized vector and scalar quantities in the development of a hazard partition model:

$$\mathbf{m} = \sum_{k=1}^{i}\left(\sum_{v_k=1}^{j}\frac{I_{v_k}}{j}\right)\mathbf{u}_k \tag{19}$$

$$\sigma_{low} = \sqrt{\sum_{k=1}^{i}\frac{\left(\overline{m} - I_k\right)^2}{i-1}},\ i \neq 1 \tag{20}$$

Equation (19) is a mean intensity vector involving indices k and v_k to perform a nested summation of image intensities. The initial partition scalar σ_{low} is constructed by taking the standard deviation of coefficients extracted from $\mathbf{m}$, the pixel intensity vector mean (over-bars indicate an arithmetic mean). Our final partition scalar is derived using a similar operational structure:

$$\boldsymbol{\sigma}_k = \sum_{k=1}^{i}\left(\sqrt{\sum_{v_k=1}^{j}\frac{\left(\overline{I}_j - I_{v_k}\right)^2}{j-1}}\right)\mathbf{u}_k,\ j \neq 1 \tag{21}$$

$$M_{mid} = \overline{\sigma}_k + 1 \tag{22}$$

Equations (19 and 21) are statistical operations used to derive lower and mid-range hazard partitions σ_{low} and M_{mid}, respectively, where M_{mid} is the mean of the image intensity standard deviation vector $\boldsymbol{\sigma}_k$. Each partition is applied to a conditional rule set for determining risk associated with viewable landing sites:

- IF $|I| \leq \sigma_{low}$, terrain is SAFE
- IF $|I| > \sigma_{low}$ AND $|I| \leq M_{mid}$, terrain is RISKY
- IF $|I| > M_{mid}$, terrain is UNSAFE

The use of absolute image intensity over signed intensity in our rule construct saves processor resources and time by

requiring only the above rules for autonomous risk determination. A slightly more involved rule set based on signed image intensity would require more time and computational resources during the brief EDL time period.

3. Results

Our descent profile involves the incorporation of a monocular camera model and various digital elevation models (DEMs) as simulation tools used to visualize and validate our vision methodology. The extraction of camera imagery for the purpose of geographical hazard assessment of landing sites functions as the initialization operation in our descent algorithm. Using an arbitrary DEM, we apply Equations (7-8) to form a spacecraft perspective view of the digital terrain.

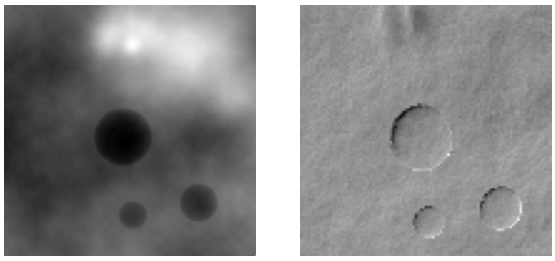

A Digital Terrain Graphic B Spacecraft Perspective

Figure 6 Extraction of Spacecraft-Camera Perspective

Imagery collected from a DEM test-bed provides an 8-bit (0-255) grayscale representation of the distant surface geography throughout the camera simulation. Equations (9-10) are used for two consecutive images taken by the spacecraft to develop a parameterized historic perspective of geographic hazards based on image intensity. Our algorithm generates imagery based on a 101×101 size image with a resolution of 5.1 m/pixel at 10 km. Pixel intensities of each camera image are used to model depth associated with the corresponding 2D perspective views of a DEM. By analyzing intensity deviations associated with each camera image we are able to develop the hazard partition model visualized in Figure 7.

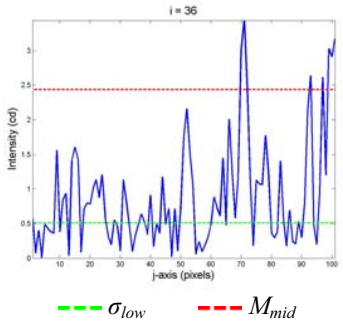

Figure 7 Hazard Partition Model: Absolute Intensity vs. v for an arbitrary image column u

Intensities less than or equal to σ_{low} are considered *safe* (■) landing sites. *Risky* (■) landing sites correspond to image intensities greater than σ_{low} and less than M_{mid}. The remaining intensities are greater than M_{mid} and represent *unsafe* (■) or hazardous landing sites. We use a pseudo-random numeric scheme to populate respective spacecraft position vectors to create the effect of a natural descent trajectory between imagery. Space coordinates $\mathbf{p_i}$ and $\mathbf{p_{i+1}}$ are then matriculated to form pixel translation coefficients for registration. By assigning former imagery as the object of transformation, we obtain the forward registration descent profile.

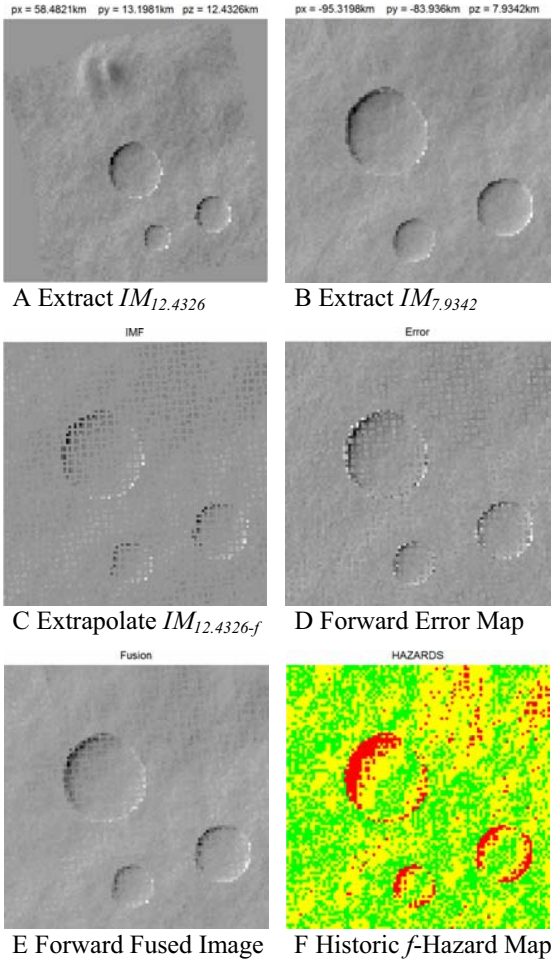

A Extract $IM_{12.4326}$ B Extract $IM_{7.9342}$

C Extrapolate $IM_{12.4326\text{-}f}$ D Forward Error Map

E Forward Fused Image F Historic *f*-Hazard Map

Figure 8 Forward Registration Historic Simulation

Subscripts above indicate spacecraft altitude (and registration type, Figure 8-C) in kilometers indicative of the atmospheric position and perspective of the vehicle at that time. By assigning latter imagery as the object of transformation, we obtain a similar pseudo-random scheme for our reverse registration descent profile. Each visualization technique is designed to provide qualitative and quantitative data in regards to safe landing site determination and module processing time.

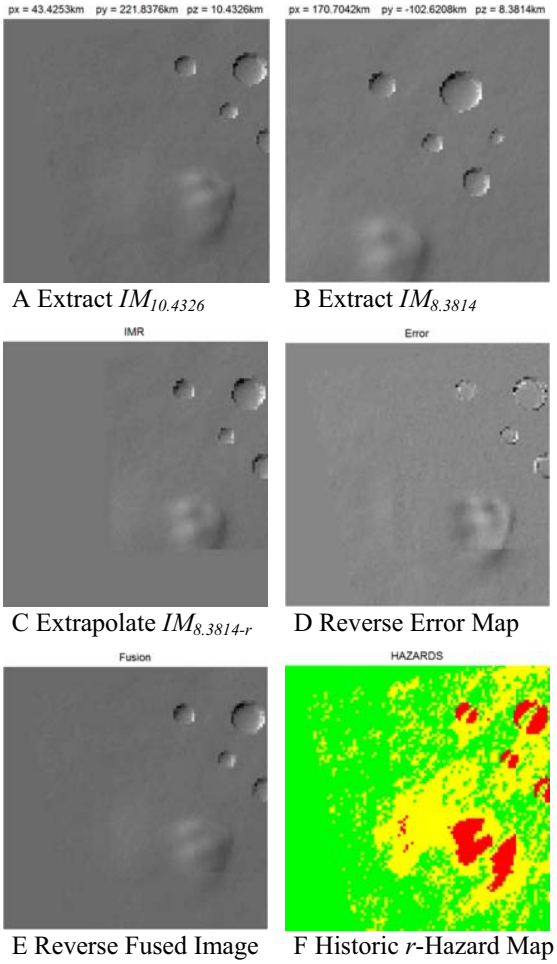

A Extract $IM_{10.4326}$ B Extract $IM_{8.3814}$

C Extrapolate $IM_{8.3814\text{-}r}$ D Reverse Error Map

E Reverse Fused Image F Historic *r*-Hazard Map

Figure 9 Reverse Registration Historic Simulation

Image extraction between coordinate systems is the most costly aspect of our algorithm (Figure 10). This is expected due to the 3D operations required to simulate and model planetary terrain. We ran a total of 50 simulation iterations (25 reverse registration profiles and 25 forward registration profiles) using a Toshiba Satellite M35x-S111: 1.5GHz Intel Celeron M Processor, 224MB RAM, Windows XP OS. Results show an average processing time of 1.767 seconds for DEM transformation to extract IM_i using reverse registration (1.663 seconds using forward registration). Similar times are recorded for collection of image IM_{i+1}: 1.675 seconds (reverse registration) and 1.641 seconds (forward registration). Average run times for 2D registration show an advantage over using a 3D methodology for cognitive descent:

- Forward Registered Image (IM_f): 154 ms
- Reverse Registered Image (IM_r): 162 ms
- Forward Fused Image: 129 ms
- Reverse Fused Image: 129 ms
- Summation of Image Operations: 451 ms

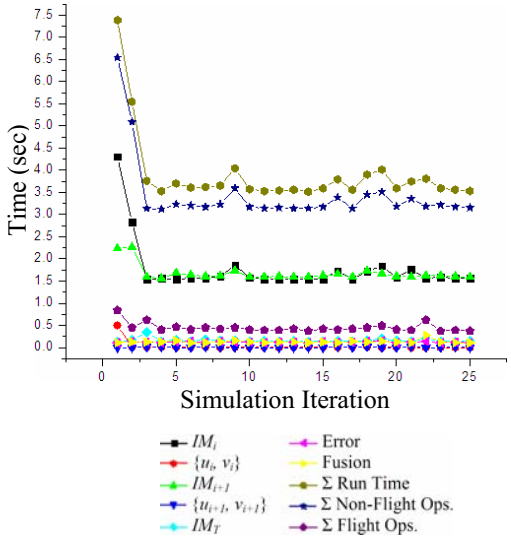

Figure 10 Autonomous Descent Operations Time Chart

4. Limitations

Albeit the availability of powerful yet costly techniques in 3D imaging and modeling applicable to this research for onboard processing, our use of such techniques as discussed in this paper are only incorporated for the development of a non-flight test-bed used for rigid body analysis and simulation of a pseudo-random descent. In reference to the transfer trajectory duration for interplanetary space travel, our processing time for autonomous operations during EDL is extremely limited, rendering costly algorithms inefficient. This constraint presents a trade-off between quantity and quality of digital imagery versus internal image processing time, which is directly proportional to the properties and amount of the surface data input: higher quantities of data of a specified quality equate to longer processing time of that data. Conversely, lower quantities of data of a specified quality equate to shorter processing time of that data. Our objective is therefore to provide a time efficient flight sequence for autonomous onboard hazard assessment based on a minimal quantity of 2D quality surface data.

Registration of terrain imagery between spacecraft coordinate systems presented a trade between the use of 2D image transformation and pixel retention for a descent profile. We noticed an increase in error for progressively aggressive positioning parameters and extremes in rotational coefficients. Full rotation about all three axes resulted in unmatched registrations due to the inherent difference between rotating about the DEM in world coordinates and rotating about the camera center in pixel coordinates, restricting our use of rotation between imagery to the z-axis. However, large variations in z-axis rotation also resulted in unmatched registrations due to

perspective projection, as shown in Figure 11 for a right angle polarity examination.

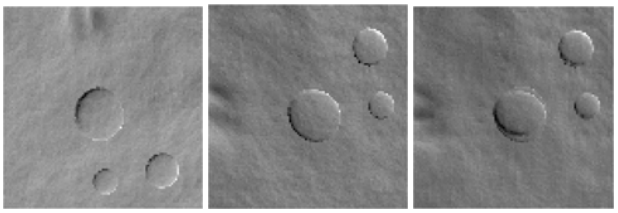

IM_i IM_{i+1} Fused Image

Figure 11 Perspective projection graphic for large z-axis variation between coordinate systems in a planar forward registration profile

5. Conclusions

Concepts presented in this paper are extracted from various techniques in computer vision, projective geometry, image processing, and 3D graphics. In multiple views for a spacecraft, there exists an image taken at iteration *i* and a second image (further in descent) taken at iteration $i + 1$. We apply a technique that computes translation and rotation transfer functions between a point in the first iteration image and the same point in the second iteration image. This allows us to derive an expression for the complete image transfer function between two image views – i.e. it allows us to place an image from one coordinate system and transform it to match the coordinate system of another image-iteration. Terrain hazards associated with the transformed images can then be calculated and integrated to provide a coherent understanding of hazard assessment for safe spacecraft landing.

6. Acknowledgements

This research was sponsored by the California Institute of Technology Minority Undergraduate Research Fellowship (MURF) and the Mars Technology Program and was conducted at the Jet Propulsion Laboratory in Pasadena, CA, under contract with the National Aeronautics and Space Administration. The digital elevation model test-bed suite was provided by Navid Serrano of JPL, whose contributions to this research are gratefully appreciated.

7. References

[1] A. Howard and H. Seraji, "Multi-Sensor Terrain Classification for Safe Spacecraft Landing," *IEEE Transactions on Aerospace and Electronic Systems*, pp. 1-8, July 2004.

[2] J. Grant, "Overview of the Landing Site Selection Process and Workshop Goals," 4th Mars Exploration Rover Landing Site Selection Workshop, Pasadena, CA., March 2003.

[3] M. Golombek, R. Cook, H. J. Moore, and T. J. Parker, "Selection of the Mars Pathfinder landing site," *Journal of Geophysical Research, Vol. 102, No. E2*, pp. 3967-3988, February 1997.

[4] A. Johnson, Y. Cheng, and L. Matthies, "Machine Vision for Autonomous Small Body Navigation," *IEEE Aerospace Conference*, 2000.

[5] M. Bajracharya, "Single Image Based Hazard Detection for a Planetary Lander," *Proceedings of the World Automation Congress*, Orlando, FL, June 2002.

[6] S. Strandmoe, T. Jean-Marius, and S. Trinh, "Toward a Vision Based Autonomous Planetary Lander", *Proceedings of the AIAA*, 1999.

[7] A. Bartoli, P. Sturm, and R. Horaud, "Projective Structure and Motion from Two Views of a Piecewise Planar Scene," *Eighth IEEE International Conference on Computer Vision*, Vancouver, BC, Canada, pp. 593-598, July 2001.

[8] G. Xu, J. Terai, and H. Shum, "A Linear Algorithm for Camera Self-Calibration, Motion and Structure Recovery for Multi-Planar Scenes from Two Perspective Images," *Proc. of IEEE Conference on Computer Vision and Pattern Recognition*, June 2000.

[9] B. Schulkin, H. Lim, N. Guzelsu, G. Jannuzzi and J. Federici, "Polarized Light Reflection From Strained Sinusoidal Surfaces," *Optical Society of America*, Vol. 42, No. 25, pp. 1-11, September 2003.

[10] A. Gruen and T. S. Huang. *Calibration and Orientation of Cameras in Computer Vision*. Germany: Springer, 2001.

[11] L. Li, Z. Feng and Y. Feng, "Accurate Calibration of Stereo Calibration for Machine Vision," *JCS&T*, Vol. 4, No. 3, pp. 147-151, October 2004.

[12] W. Kim, "Computer Vision Assisted Virtual Reality Calibration," *IEEE Transactions on Robotics and Automation*, pp. 1-35, June 1999.

[13] Z. Zhang, R. Deriche, O. Faugeras and Q. Luong, "A Robust Technique for Matching Two Uncalibrated Images Through Recovery of Their Unknown Epipolar Geometry," *Institut National de Recherche en Informatique et en Automatique*, Programme 4, pp. 3-43, May 1994.

[14] Y. Cheng, A. Johnson, L. Matthies, and A. Wolf, "Passive Imaging Based Hazard Avoidance for Spacecraft Safe Landing," *i-SAIRAS*, Montreal, Canada, 2001.